Nanoscale

PAPER

View Article Online
View Journal | View Issue

Cite this: *Nanoscale*, 2022, **14**, 5369

Observation of high-density multi-excitons in medium-size CdSe/CdZnS/ZnS colloidal quantum dots through transient spectroscopy and their optical gain properties†

Hongyu Yang,[a] Si Li,[b] Lei Zhang,[a] Wenbin Xiang,[a] Yi Zhang, *[c] Xiaoyong Wang,*[b] Min Xiao,[b,d] Yiping Cui [a] and Jiayu Zhang *[a]

Received 9th February 2022,
Accepted 5th March 2022

DOI: 10.1039/d2nr00761d

rsc.li/nanoscale

Semiconductor quantum dots have extremely significant advantages in terms of optoelectronic devices. However, it is unfeasible to avoid the generation of charged exciton states during operation. Such states can change the radiation recombination rate and bring additional non-radiative Auger recombination channels. Herein, we synthesize high photoluminescence quantum yield medium-size CdSe/CdZnS/ZnS core/alloy shell/shell QDs. Their multiexciton spectra and dynamics were systematically studied by pump-power-dependent fluorescence blinking and time-correlated spectroscopy. The lifetimes of positively/negatively charged trions and biexcitons are estimated to be 0.74/6.1 and 0.16 ns, respectively. It demonstrated that the band-edge biexciton is influenced by the Coulomb interaction and Stark effect. The amplified spontaneous emission threshold is only 81 μJ cm^{-2} and can retain a long operation lifetime under continuous pumping. A vertical microcavity surface-emitting laser device is fabricated using these QDs. The coupling factor between the spontaneous emission and cavity mode is 0.81, which benefits the low stimulated emission threshold. This work provides a new perspective of the charged states in the multiexciton AR process in the QDs, implying a promising application prospect of such QDs as optical gain materials in "zero-threshold" laser fabrication.

Introduction

Semiconductor quantum dots (QDs) have excellent photoelectric properties and are widely studied and applied in light-emitting diodes,[1] solar cells, and full-color laser devices.[2–5] For these materials, dynamic processes of multiexcitons or charged excitons have drawn much attention, which is of great significance in improving the performance of these devices, especially under intense working conditions.[6–8] The non-radiative Auger recombination (AR) of multiexcitons of QDs is substantially more effective than the corresponding bulk materials due to the strong quantum confinement energy in QDs and the lifted momentum conservation restriction. In addition, the efficiency roll-off of QD LEDs at a high current density has been attributed to the non-radiative AR of extra electron charging states.[9,10]

There are two main strategies for suppressing the AR of multiexcitons, that is, (1) by adjusting the geometric structure of QDs[11,12] (*e.g.* changing the shape and size of the core or the shell) and (2) adding an alloy layer between the core and the shell.[13,14] In addition, recent studies have shown that the dielectric screening effect related to the size of QDs and the shell thickness can significantly influence the Auger recombination of charged single excitons (also called trions). Due to the different localizations of electron/hole wavefunctions, their surrounding dielectric environments are significantly different. Therefore, the AR of positive/negative trions can be considerably different due to different screening degrees *via* varying the core size and shell thickness, which indicates that the multiexciton recombination of QDs can be adjusted through this dielectric screening effect.

The stability of QDs can be significantly improved by shelling with wide bandgap ZnS (E_g = 3.75 eV) materials, which has been proven in type-II systems such as ZnSe/CdS/ZnS[15,16] and alloy core/shell systems such as ZnCdS/ZnS.[17] Moreover, the electron/hole wavefunction can be confined away from the

[a]*Advanced Photonic Center, School of Electronic science and Engineering, Southeast University, Nanjing 210096, China. E-mail: jyzhang@seu.edu.cn*
[b]*National Laboratory of Solid State Microstructures, College of Engineering and Applied Sciences, and School of Physics, Nanjing University, Nanjing 210093, China. E-mail: wxiaoyong@nju.edu.cn*
[c]*College of Energy and Electrical Engineering, Hohai University, Nanjing, 210098, China. E-mail: zynjjs@outlook.com*
[d]*University of Arkansas, Fayetteville, Arkansas 72701, USA*

†Electronic supplementary information (ESI) available: Supplementary Notes S1–S3, Table S1 and Fig. S1–S6. See DOI: 10.1039/d2nr00761d

surface benefiting from the large dielectric constant of ZnS (ε_r = 5.69). Therefore, the dielectric screening effect is enhanced and effectively suppresses the Auger process of trions without changing the locality of the wavefunction. On the other hand, the components of QDs can be adjusted to make an alloy core or gradient shell, expanding the spectral range through excellent band engineering.[18,19] Meanwhile, the interfacial defects caused by lattice mismatch between the core and the shell (for example, CdSe and ZnS, ~12%) can be effectively suppressed. This smooth interfacial barrier can also significantly reduce the contribution of the sharp radial edge of the electron/hole wavefunction to the high momentum components, reducing the Auger recombination rate by about 3–10 times.[20,21]

It has been shown that the charge states in QDs could contribute to the low-threshold optical gain.[22–24] However, the dynamics concerning the charge state are still not well understood. Herein, high-QY CdSe/CdZnS/ZnS medium-size QDs were introduced and their multi-exciton dynamics through systematic pump intensity-dependent single-dot fluorescence blinking, time-resolved fluorescence spectroscopy and amplified spontaneous emission (ASE) measurements were investigated. The trion and biexciton dynamics were verified at first, and the continuous red-shift of the band-edge emission and shortened emission lifetime were observed along with the increase of the pump power. The high-order exciton Auger ionization effect was identified as the origin of these phenomena since the remaining charge can change the dielectric environment and provide additional AR channels on band-edge biexcitons. These QDs were also exploited as a gain medium to fabricate a VCSEL and the laser was realized with a low threshold of 41.5 μJ cm^{-2}.

Results and discussion

Structural and optical characterization

CdSe/CdZnS/ZnS core/multi-shell QDs with a gradient interface were prepared following the "one-pot" method from ref. 25. The alloy shell was coated on the surface of the CdSe core by the difference in the reactivity of the Cd/Zn and sulfur precursor (1-dodecanethiol, DDT) at a high temperature. The outermost ZnS shell could provide dielectric screening to confine the exciton wavefunction from interacting with surface states. The QD particles remain mostly as spheres as shown in their TEM images (Fig. 1a) with an excellent size dispersity of 6.55 ± 1 nm. Fig. 1b and Fig. S1† show the representative HRTEM images. The (111) lattice spacing can be calculated as 3.41 Å and the corresponding fast Fourier transform pattern shows a single dot projected in the (111) direction in Fig. 1(c), indicating the zinc-blende structure. The X-ray diffraction (XRD) patterns shown in Fig. 1(d) are consistent with the TEM analysis. The steady-state absorption and photoluminescence spectra

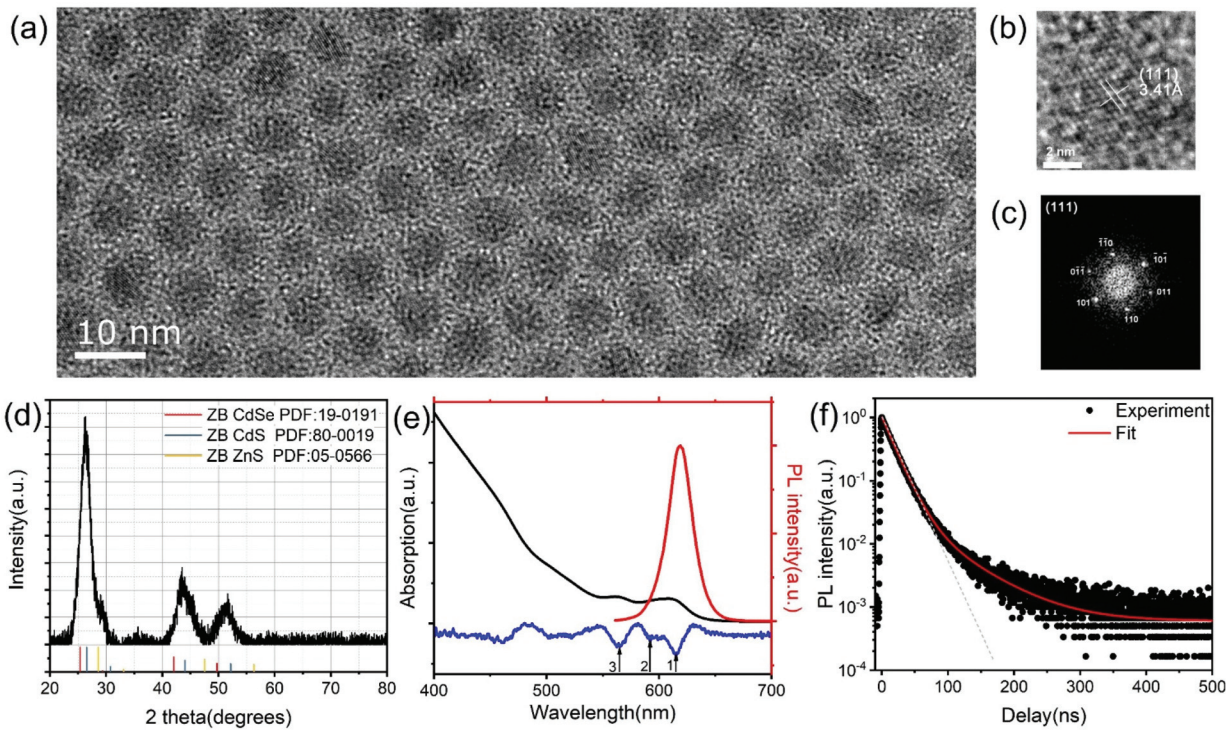

Fig. 1 (a) TEM image of the CdSe/CdZnS/ZnS QDs. Scale bar: 10 nm. (b) HRTEM image. Scale bar: 2 nm. The lattice spacing (~0.341 nm) corresponds to the (111) plane of the zinc blende structure. (c) Corresponding FFT pattern projected in the (111) direction. (d) XRD pattern of the QDs. The standard powder diffraction patterns of the zinc blende structure of CdSe, CdS and ZnS are shown for comparison. (e) The UV-vis absorption and PL spectra. The blue line is the second-derivative of the absorption spectrum. The arrows mark the $1S_e$–$1S_{3/2}$, $1S_e$–$2S_{3/2}$, and $1P_e$–$1P_{3/2}$ transitions. (f) PL decay curve and the corresponding fit. The grey dashed line represents the band-edge exciton recombination.

were measured as shown in Fig. 1(e), where the PL peak is located at 618 nm with a full width at half-height (FWHM) of 26 nm. The $1S_e$–$1S_{3/2}$ transition located at 615 nm can be well-observed in the absorption spectrum, which indicates the corresponding Stokes shift of 3 nm arising from the strong quantum confinement in type-I QDs. A closer look at the second-derivative curve of the absorption spectrum (blue line) reveals that another two well-pronounced peaks at 592 and 564 nm are found. The energy differences with $1S_e$–$1S_{3/2}$ absorption peaks are 79 and 179 meV, respectively, and are assigned to $1S_e$–$2S_{3/2}$ and $1P_e$–$1P_{3/2}$ transitions. The structure of low-energy electronic states derived from this analysis is shown in the inset of Fig. 1(e). The PLQY of the QD solution is high up to 80%. Fig. 1(f) shows the PL decay curve measured by the time-correlated single-photon counting method. The decay curve can be well-fitted by a bi-exponent decay function as below:

$$I(t) = A_1 e^{-\frac{t}{\tau_1}} + A_2 e^{-\frac{t}{\tau_2}} + I_0 \quad (1)$$

where the short-lived component τ_1 represents the direct radiative recombination of excitons, and the long-lived component τ_2 represents the interaction between the excitons and surface defects.[26,27] Through fitting, τ_1 = 17.38 ns and τ_2 = 61.44 ns, and the weights are 87.2% and 12.81%, corresponding to the average life τ_{av} = 19.14 ns. This indicates that the probability of excitons through inter-band recombination is far greater than the interaction with surface states since the wide bandgap ZnS shell provides effective exciton confinement.

Single-dot fluorescence blinking and dynamics

The typical single-dot fluorescence time trajectories and the corresponding intensity distribution histogram under excitation powers of 50, 100 and 200 nW are shown in Fig. 2. To prevent the QDs from being bleached by continuous excitation during the experiment and collect sufficient experimental data, the highest excitation power of 200 nW was used (corresponding to a power density of about 25 μJ cm^{-2} and an average exciton number $\langle N \rangle$ of 0.08). The "on" states almost occupied the PL trajectory and few "off" states were found for the lowest excitation power of 50 nW, which is related to the restricted interaction between the surface defects and excitons. With increasing the pump power to 100 and 200 nW, the intensity distribution histograms become asymmetric and are fitted with three Gaussian functions. The intensity of the newly emerging states is higher than the background noise, and the probability increases with the pump power, corresponding to "grey" and "mix" states ("off" and a few "grey" states, due to the overlapping in the histograms). For the single-dot fluorescence measurement, the "grey" state comes from the radiative recombination of negative trions, and the "off" state comes from the trapped excitons and the strong non-radiative AR of positive trions.[28,29] Furthermore, we analysed the fluorescence decay curves of different states. The decay curve of "on" states recorded at 50 nW and 200 nW in Fig. 3 can be fitted by a single-exponent decay function with a constant of 16.65 ns, which is similar to the lifetime measured in the ensemble. The "grey" states' decay curve in Fig. 3(b) can be fitted with a single-exponent function with a constant of 6.27

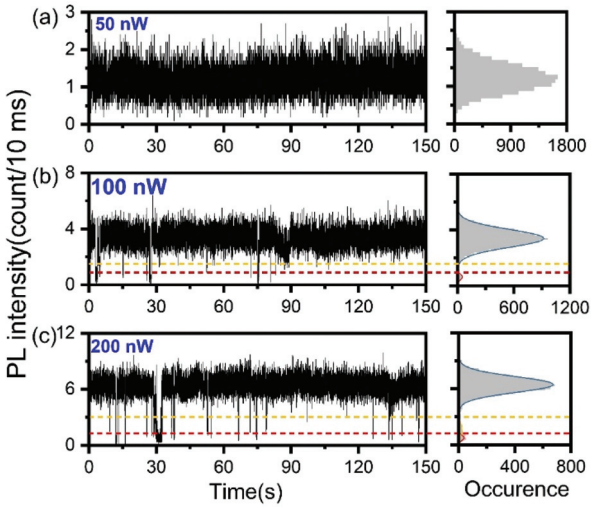

Fig. 2 (a)–(c) The typical single-dot fluorescence intensity trajectories (left) and their corresponding intensity distribution histograms (right). The histograms in (b) and (c) are fitted with three Gaussian functions. The yellow and red dashed lines are the "grey" and "mix" state thresholds. Binning time: 10 ms.

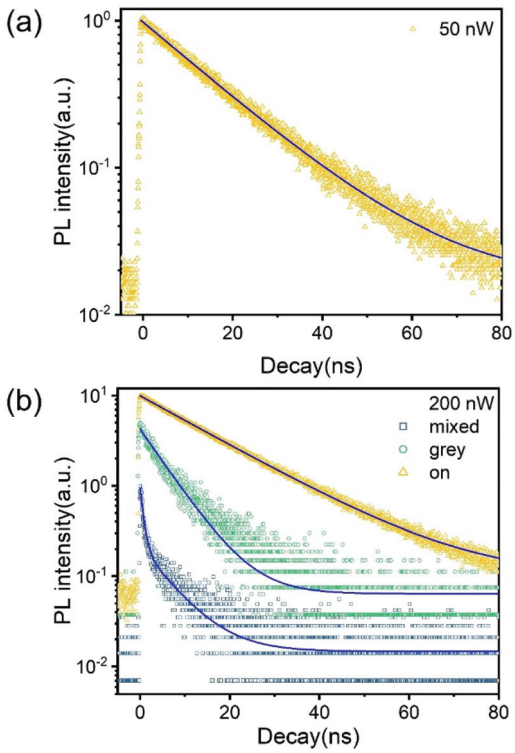

Fig. 3 PL decay curves (dots) of a single dot and their corresponding fit (blue lines). (a) Pump power of 50 nW and (b) "mix", "grey" and "on" states measured with a pump power of 200 nW. For clarity, the three curves for a certain amount of translation in the longitudinal axis are shown.

ns. The decay curve of "mix" states can be well-fitted using a double-exponent function with constants of 6.1 and 0.74 ns, where the short lifetime corresponds to the Auger recombination of positive trions.[30] The residuals are shown in Fig. S2† and the adjusted (R^2) values are more than 0.985.

Biexciton and higher-order multiexciton dynamics

To further investigate the multiexciton dynamics, we measured the time-correlated photoluminescence spectra of the QD ensemble under intense pumping using a streak camera system. During the measurement, the solution was vigorously agitated to reduce the effect of photoionization.[13] The PL decay curves in Fig. 4(a) were extracted from their corresponding streak camera images and were tail-normalized so that they coincided with a long decay time (t > 3 ns).[31] At this stage, the multiexcitons have decayed, and the remaining fluorescence is mainly determined by single excitons and trions. The average exciton number $\langle N\rangle$ excited right after the ultra-short pulse excitation can be fitted using the equation as below:

$$I_{\text{long}} \propto 1 - e^{-\langle N\rangle} = 1 - e^{-j\delta_{\text{abs}}} \quad (2)$$

where I_{long} is the PL intensity at t = 3 ns in Fig. 4(c), j is the photon number per square centimeter per pulse and δ_{abs} is the absorption cross-section at 400 nm. The absorption cross-section of 6×10^{-15} cm^2 was derived by fitting with eqn (2).

The biexciton and trion dynamics were extracted from the tail-normalized decay curves of $\langle N\rangle$ = 0.1 and 0.01, as shown in Fig. 4(b). The probability that the number (n) of excitons in QDs, $P(n)$, obeys the Poisson distribution[32] is as below:

$$P(n) = \frac{\langle N\rangle^n}{n!} e^{\langle N\rangle} \quad (3)$$

The probabilities that n is 0, 1, 2, and >2 can be calculated as 0.9048, 0.0905, 0.0045, and 0.0002 when $\langle N\rangle$ = 0.1, respectively, indicating that high-order exciton contribution can be neglected. The biexciton lifetime is estimated to be 150.8 ps. We can deduce that the biexciton AR lifetime $\tau_{xx,A}$ = 153 ps and quantum yield QY_{xx} = 2.6% (ESI Note S1†). The trion and biexciton lifetimes of the CdSe/CdZnS/ZnS QDs are relatively longer than those of similar size QDs shown in ESI Table S1,† proving the suppression of non-radiative AR probability.

At a higher pump intensity ($\langle N\rangle$ > 0.46), another peak appeared at the high-energy shoulder of the single-exciton spectra located at 580 nm, as shown in Fig. 4(d) and Fig. S3.† The difference between this peak and the peak of the single exciton spectrum is about 42 nm (131 meV) and is 16 nm (60 meV) different from the $1P_e$–$1P_{3/2}$ transition. Based on previous research and the absorption peak, we believe that this emission comes from the high-level (1P) exciton emission.[33] At this stage, the double-degenerate 1S energy level of some QDs is filled, and the higher-order excitons ($N \geq 3$) can occupy a higher energy level (1P, 1D, *etc.*). The radiative lifetime of the 1P transition is about 38 ps and the large binding energy may be derived from the polarization characteristics of the 1P energy level.[34] The 1D excitons were not observed in these QDs even though the measured $\langle N\rangle$ value is up to 7.8. In these sized QDs, the wavefunction overlap between the highly excited electrons and holes is high such that the high-level excitons are more prone to non-radiative AR.

The PL spectra with a delay window of 0–100 ps after the ultra-short pulse excitation were extracted, as shown in Fig. S4.† With the increasing pump intensity, we observed an apparent redshift of the band-edge emission spectra in the initial stage. To verify the origin of this shift, we calculated the biexciton spectra in Fig. 4(e) according to the spectra acquired at low pump intensities ($\langle N\rangle$ = 0.1 and 0.01, see ESI Note S2†). The biexciton peak is redshifted by 21 meV compared to the neutral single excitons, corresponding to the biexciton binding energy (Δ_{XX} = −21 meV) of similar size CdSe QDs due to the Coulomb attractions of excitons and the intrinsic Stark effect.[32,35] The trion spectra were also measured in the single-dot spectra at 200 nW, as shown in Fig. S5.† The trion PL spectra were determined according to the differences in the intensities of the neutral single excitons, thus producing a trion binding energy of +13 meV. In addition, the 1P transition is far away from the band-edge emission. Therefore, the observed redshift must result from other mechanics.

The multiexciton AR process can also bring the Auger ionization, which excites the electrons/holes produced by the Auger recombination out of the QDs to generate charged excitons. In the interaction formalism, the electron–hole Coulomb interaction increases the probability of AR and influences the band-edge emission due to the instrinsic quantum-confined

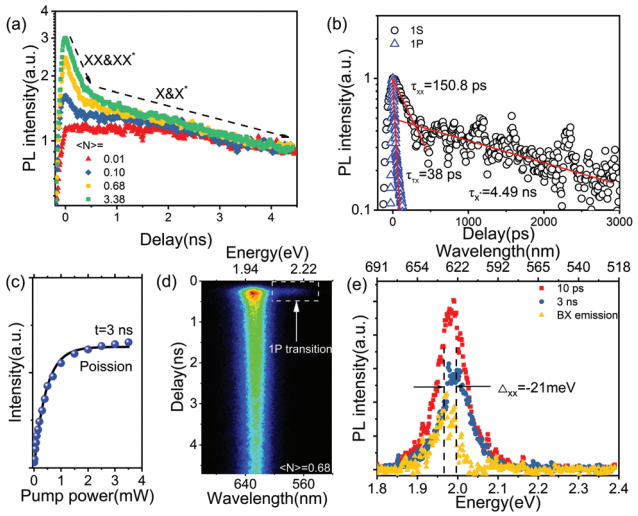

Fig. 4 (a) PL decay curves with different $\langle N\rangle$ values. At the early stage, the decay was controlled by the AR process of neutral and charged biexcitons. Afterward, long decay is mainly from trions and neutral single excitons; (b) PL decay curves of biexcitons, trions and triexcitons (dots) and their corresponding decay process (red lines); (c) PL intensity at a time delay of 3 ns as a function of pump power and $\langle N\rangle$ and the fitted curve; (d) streak image of $\langle N\rangle$ = 0.68; and (e) the extracted spectra from the streak camera image of $\langle N\rangle$ = 0.1 at delays of 10 ps (red dotted line) and 3 ns (blue dotted line). The yellow dotted line is the calculated biexciton spectra and the corresponding biexciton binding energy Δ_{xx} = −21 meV.

Stark effect (QCSE). As the pump intensity increases, the probability of high-order exciton generation increases as well as the charge states. The binding energy of charged biexcitons thus increases arising from the enhanced dielectric screening effect and Coulomb attraction. In addition, the decay curve of the 1S energy level in Fig. 4(a) with the increase of pump power has a steeper slope in the early delay window which means that the inter-band emission becomes faster. These results indicate that the energy and recombination dynamics of biexcitons is affected by the unbalanced charge. According to the above analysis, the highly excited charge can participate in the AR process, and the AR process is accelerated since more AR channels are open under intense pumping.

Amplified spontaneous emission and optical gain

Even though the non-radiative AR is proved to be suppressed in these medium-size QDs, the ASE process, including the optical gain lifetime, is still a concern. ASE is observed by exciting spin-coating films using femtosecond pulses and monitoring emissions from the film edge. Fig. 5(a) shows the typical pump-power-dependent PL spectra. The broadband spontaneous emission is observed at low pump intensities, while a sharp ASE peak (FWHM = ~8–9 nm) appears on the red-shoulder of the emission band at higher pump fluences. The redshift arises from the attractive Coulomb attraction of biexcitons and the optical mode of the film.[36] The plots of pump-power-dependent integrated PL intensity in Fig. 5(b) indicate an ASE threshold of ~81 μJ cm^{-2}, above which a super-linear emission intensity increase appears. However, the 1P transition was not observed, which may result from the rapid AR of the 1P transition, which consumes the excitons at this energy level; thus the establishment time of the 1P ASE is shorter than the gain lifetime.[32] The ASE transient spectra were measured, as shown in Fig. 5(c), and the corresponding decay curves were extracted in Fig. 5(d). When the pump intensity is low, only a broad-spectrum of long-lived spontaneous emissions is observed. Once the power exceeds the threshold, a narrow-band ASE spectrum appears, and its lifetime rapidly decreases to ~13 ps, which is about 12 times faster than the biexciton AR lifetime, which is close to the resolution limit of the streak camera system. The ASE stability was also measured under continuous laser irradiation at 300 μJ cm^{-2} in Fig. S6.† The ASE intensity can maintain more than 80% of its initial intensity after 60 min (3×10^6 shots) pumping. These results prove that these medium-size QDs are excellent and extremely stable gain materials, and monochromatic laser devices can be made.

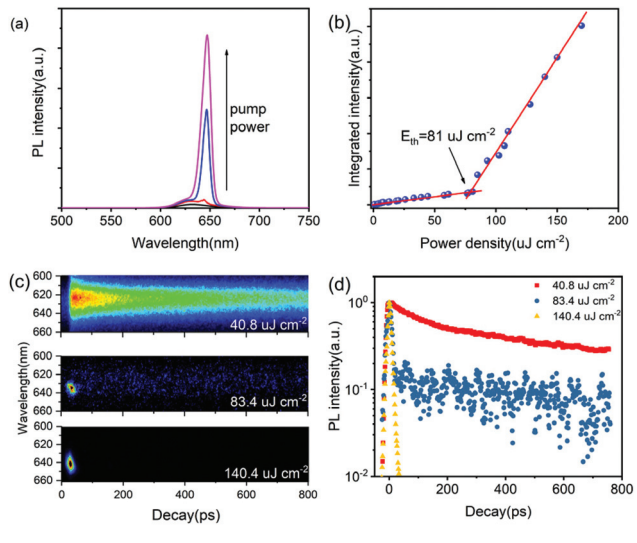

Fig. 5 (a) The PL emission of QDs' film under different pump powers; (b) integrated PL intensity as a function of pump power; (c) the streak camera images of QDs' film under different pump powers; and (d) decay curve extracted from (c).

Single-mode laser devices from a VCSEL

To further prove the effective stimulated emission from these QDs, a VCSEL device was made and proven to lase (see the Experiment section). The reflective and PL spectra of the microcavity are shown in Fig. 6(a). A "dip" (λ_0 = ~650 nm) appears in the photonic bandgap, which is apparent in the Fabry–Perot cavity resonance mode.[37] The PL FWHM is about ~9.8 nm and the peak is located at the "dip", proving that the cavity mode matches well with the spontaneous emission. Fig. 6(b) shows the PL decay curves of the spontaneous emission of the microcavity and bare QD film. The decay curves can all be fitted with a bi-exponential function. The fast decay component corresponds to spontaneous recombination and the slow decay is likely due to other radiative decay channels. Spontaneous emission is essential in analysing microcavity dynamics because the rate and probability can be modulated by the Purcell effect of the microcavity.[39] The spontaneous life-

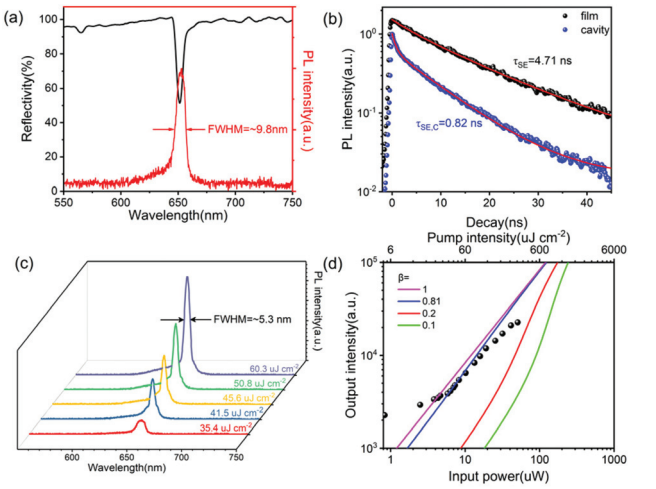

Fig. 6 (a) Reflective and fluorescence spectra of the microcavity; (b) PL decay curves of the bare QDs' film and microcavity, where the red lines are the corresponding bi-exponential fit; (c) the microcavity emission spectra with the increasing pump intensity; and (d) the dots show the log–log plot of the L–L curve. The blue line is the corresponding fit using the coupled rate function and a β-factor of ~0.81 is obtained. The other lines are calculated for other β-factors for comparison.

time of the microcavity ($\tau_{SE,C}$ = 0.82 ns) is considerably shorter than that of the QD film (τ_{SE} = 4.71 ns), which proves that the spontaneous emission is accelerated by the microcavity mode. The effective Purcell factor can be determined by the ratio of these lifetimes:

$$F_P = \frac{\tau_{SE}}{\tau_{SE,C}} = 5.74 \quad (4)$$

The stimulated emission of the as-fabricated microcavity was proved by monitoring the emission spectra as the pump intensity was increased as shown in Fig. 6(c). After the pump intensity exceeds the threshold, an emission peak located at 652.14 nm with an FWHM of ~5.3 nm appears above the spontaneous emission and becomes dominant afterward, which indicates the laser emission. The well-defined laser spot is shown in Fig. S7.† We plotted the integrated PL intensity *versus* pump power in the form of a logarithmic graph (light-in/light out curve, L–L curve) in Fig. 6(d). The L–L curve was fitted with the traditional laser rate function (see ESI Note S3†), which gives a "soft" threshold appearing at ~8 μW and a high coupling factor (β-factor) of 0.81 between the cavity mode and spontaneous emission. This indicates that the large fraction of spontaneous emission is coupled into the cavity, from which the ultra-low average exciton number threshold is obtained. In addition, the considerable enhancement means that QDs can support higher exciton densities before Auger recombination begins to compete with optical gain.[38] The threshold was calculated as 40.8 μJ cm^{-2} (corresponding to $\langle N \rangle$ = 0.5) when the radius of the pump laser was 70 μm.

Conclusion

In conclusion, neutral and charged exciton/biexciton dynamics were systematically studied in high-quality medium-size CdSe/CdZnS/ZnS core/alloy shell/shell QDs. The QDs show suppressed non-radiative AR and highly effective Auger ionization under intense pumping. The charge states alter the biexciton energy due to the intrinsic QCSE and accelerate the band-edge carrier decay as a result of introducing extra AR channels. Furthermore, the medium size QDs have highly efficient and stable optical gain properties. An F–P microcavity device was made, from which the low stimulated emission threshold was achieved. This could be ascribed to a huge β-factor of 0.81 and a Purcell factor of 5.74. This work provides a new perspective of the charged states in the multiexciton transient process in the QDs, implying a promising application prospect of such QDs as optical gain materials in "zero-threshold" microcavity laser fabrication.

Experiment

Materials

Cadmium oxide (CdO, 99.99%), tri-*n*-octylphosphine (TOP, 97%), sulfur powder (99.9%) and 1-dodecanethiol (DDT, 98%) were purchased from Sigma-Aldrich. Se powder (200 mesh, 99%) and 1-octadecene (ODE, 90%) were purchased from Alfa Aesar. All the chemical materials were used without further purification procedures.

QDs synthesis

CdSe/CdZnS/ZnS core/alloy shell/shell QDs were synthesized using the method published by Bae *et al.*[25] The QDs were washed with ethanol and acetone at least three times to remove unreacted precursors and by-products. The QDs were finally dissolved in toluene for further experiments.

Sample characterization

The solution absorption spectrum was recorded using a Shimadzu UV-3600 ultraviolet-vis spectrophotometer. The solution PL spectrum and PL decay curve were recorded using a HORIBA FM-4P-TCSPC spectrometer. The PLQY was measured by comparison with standard Rhodamine B. The TEM images were recorded using a JOEL company JEM-2100 electron microscope. XRD patterns were obtained using a Bruker D8-discover X-ray diffractometer with Cu Kα radiation (λ = 1.5418 Å). Samples were prepared by thick film deposition on a quartz substrate.

The single-dot fluorescence traces were measured with a confocal microscope. The sample was prepared by mixing the diluted QDs' toluene solution and polylactic acid solution and then spin-coating on a quartz cover glass. The excitation light source was an EXR-15 Picoseconds pulsed laser (405 nm, 5 MHz) from NKT Photonics. The excitation light was focused on the sample through a 100× oil lens, and the fluorescence signal was collected through the same oil lens, and sent to a CCD camera for fluorescence spectrum measurement after passing through a 0.5 m spectrometer. The single-point fluorescence signal can also be sent to two APDs through a non-polarization-selective 50/50 beam splitter for time-dependent single-photon counting measurement. The minimum time resolution of time-dependent single-photon counting was about 250 ps.

The multiexciton dynamics of QDs were measured with an electrically triggered streak camera (Hamamatsu C5680). The excitation light was a tunable Ti:sapphire laser system with a β-BBO frequency-doubling crystal (400 nm, 150 fs, 1 kHz, Coherent LegendF-1k). For ASE measurement, the QD solution was spin-coated on a pre-cleaned glass substrate. The excitation light (400 nm, 150 fs, 1 kHz) was vertically focused on the film's surface through a cylindrical lens (10 cm focal length). The emission spectrum was measured at the edge of the film with an optical multichannel analyser (OMA, Spectrapro-300i, Acton Research Corporation). The transient spectra were measured with a Hamamatsu C5680 streak camera working in synchro scan mode.

To fabricate a microcavity device, we first spin-coated a dense QDs solution on a bottom distributed Bragg reflector (DBR). The bottom DBR was washed with deionized water, acetone and ethanol successively under ultrasonication. We used the electron beam thermal evaporation method to evaporate SiO_2

(100 nm) and Ag (50 nm) under a vacuum chamber pressure less than 1×10^{-3} Pa. To increase the adhesion between the Ag and SiO_2 layers, about 1 nm Cr was vapor-deposited before Ag. The microcavity was pumped with the aforementioned femtosecond laser, which is focused on the microcavity through a lens of 5 cm focal length. A Spectrapro-300i optical multichannel analyser was then used to collect the signal. The spontaneous emission lifetime of the microcavity is pumped by the femtosecond laser described above and measured by the mentioned streak camera working in single sweep mode.

Conflicts of interest

The authors declare no competing financial interest.

Acknowledgements

This work was supported by the Scientific Research Foundation of Graduate School of Southeast University (YBPY2024), the National Natural Science Foundation of China (62004060 and 62175029), and the Science and Technology Support Program of Jiangsu Province (BE2018117).

Notes and references

1 R. Heitz, M. Veit, A. Kalburge, Q. Xie, M. Grundmann, P. Chen, N. N. Ledentsov, A. Hoffmann, A. Madhukar, D. Bimberg, V. M. Ustinov, P. S. Kop'ev and Z. I. Alferov, *Phys. E*, 1998, **2**, 578–582.
2 Y. S. Park, J. Roh, B. T. Diroll, R. D. Schaller and V. I. Klimov, *Nat. Rev. Mater.*, 2021, **6**, 382–401.
3 R. L. Wang, Y. Q. Shang, P. Kanjanaboos, W. J. Zhou, Z. J. Ning and E. H. Sargent, *Energy Environ. Sci.*, 2016, **9**, 1130–1143.
4 C. R. Kagan, E. Lifshitz, E. H. Sargent and D. V. Talapin, *Science*, 2016, **353**(6302), 885.
5 Y. Zhang, X. Jia, S. Liu, B. Zhang, K. Lin, J. Zhang and G. Conibeer, *Sol. Energy Mater. Sol. Cells*, 2021, **225**, 111073.
6 J. M. Pietryga, Y. S. Park, J. H. Lim, A. F. Fidler, W. K. Bae, S. Brovelli and V. I. Klimov, *Chem. Rev.*, 2016, **116**, 10513–10622.
7 P. Kambhampati, *J. Phys. Chem. Lett.*, 2012, **3**, 1182–1190.
8 A. L. Efros and L. E. Brus, *ACS Nano*, 2021, **15**, 6192–6210.
9 W. K. Bae, Y. S. Park, J. Lim, D. Lee, L. A. Padilha, H. McDaniel, I. Robel, C. Lee, J. M. Pietryga and V. I. Klimov, *Nat. Commun.*, 2013, **4**, 2661.
10 B. N. Pal, Y. Ghosh, S. Brovelli, R. Laocharoensuk, V. I. Klimov, J. A. Hollingsworth and H. Htoon, *Nano Lett.*, 2012, **12**, 331–336.
11 F. J. Fan, O. Voznyy, R. P. Sabatini, K. T. Bicanic, M. M. Adachi, J. R. McBride, K. R. Reid, Y. S. Park, X. Y. Li, A. Jain, R. Quintero-Bermudez, M. Saravanapavanantham, M. Liu, M. Korkusinski, P. Hawrylak, V. I. Klimov, S. J. Rosenthal, S. Hoogland and E. H. Sargent, *Nature*, 2017, **544**, 75–79.
12 A. Jain, O. Voznyy, S. Hoogland, M. Korkusinski, P. Hawrylak and E. H. Sargent, *Nano Lett.*, 2016, **16**, 6491–6496.
13 W. K. Bae, L. A. Padilha, Y. S. Park, H. McDaniel, I. Robel, J. M. Pietryga and V. I. Klimov, *ACS Nano*, 2013, **7**, 3411–3419.
14 F. Garcia-Santamaria, S. Brovelli, R. Viswanatha, J. A. Hollingsworth, H. Htoon, S. A. Crooker and V. I. Klimov, *Nano Lett.*, 2011, **11**, 687–693.
15 C. M. Tyrakowski, A. Shamirian, C. E. Rowland, H. Y. Shen, A. Das, R. D. Schaller and P. T. Snee, *Chem. Mater.*, 2015, **27**, 7276–7281.
16 S. Wang, J. J. Li, Y. B. Lv, R. L. Wu, M. Xing, H. B. Shen, H. Z. Wang, L. S. Li and X. Chen, *Nanoscale Res. Lett.*, 2017, **12**, 380.
17 B. Guzelturk, Y. Kelestemur, M. Z. Akgul, V. K. Sharma and H. V. Demir, *J. Phys. Chem. Lett.*, 2014, **5**, 2214–2218.
18 H. J. Cao, J. L. Ma, L. Huang, H. Y. Qin, R. Y. Meng, Y. Li and X. G. Peng, *J. Am. Chem. Soc.*, 2016, **138**, 15727–15735.
19 H. B. Shen, Q. Gao, Y. B. Zhang, Y. Lin, Q. L. Lin, Z. H. Li, L. Chen, Z. P. Zeng, X. G. Li, Y. Jia, S. J. Wang, Z. L. Du, L. S. Li and Z. Y. Zhang, *Nat. Photonics*, 2019, **13**, 192–197.
20 G. E. Cragg and A. L. Efros, *Nano Lett.*, 2010, **10**, 313–317.
21 G. A. Beane, K. Gong and D. F. Kelley, *ACS Nano*, 2016, **10**, 3755–3765.
22 J. H. Yu, S. Shendre, W. K. Koh, B. Q. Liu, M. J. Li, S. Y. Hou, C. Hettiarachchi, S. Delikanli, P. Hernandez-Martinez, M. D. Birowosuto, H. Wang, T. Sum, H. V. Demir and C. Dang, *Sci. Adv.*, 2019, **5**, eaav3140.
23 J. Roh, Y. S. Park, J. Lim and V. I. Klimov, *Nat. Commun.*, 2020, **11**, 271.
24 K. F. Wu, Y. S. Park, J. Lim and V. I. Klimov, *Nat. Nanotechnol.*, 2017, **12**, 1140–1147.
25 W. K. Bae, J. Kwak, J. Lim, D. Lee, M. K. Nam, K. Char, C. Lee and S. Lee, *Nano Lett.*, 2010, **10**, 2368–2373.
26 B. Huang, H. Y. Yang, L. Zhang, Y. F. Yuan, Y. P. Cui and J. Y. Zhang, *Nanoscale*, 2018, **10**, 18331–18340.
27 Y. Niu, C. D. Pu, R. C. Lai, R. Y. Meng, W. Z. Lin, H. Y. Qin and X. G. Peng, *Nano Res.*, 2017, **10**, 1149–1162.
28 P. P. Jha and P. Guyot-Sionnest, *ACS Nano*, 2009, **3**, 1011–1015.
29 F. R. Hu, Q. Zhang, C. F. Zhang, X. Y. Wang and M. Xiao, *Appl. Phys. Lett.*, 2015, **106**, 133106.
30 Y. S. Park, W. K. Bae, J. M. Pietryga and V. I. Klimov, *ACS Nano*, 2014, **8**, 7288–7296.
31 F. Garcia-Santamaria, Y. F. Chen, J. Vela, R. D. Schaller, J. A. Hollingsworth and V. I. Klimov, *Nano Lett.*, 2009, **9**, 3482–3488.
32 J. M. Caruge, Y. T. Chan, V. Sundar, H. J. Eisler and M. G. Bawendi, *Phys. Rev. B: Condens. Matter Mater. Phys.*, 2004, **70**, 085316.
33 A. Franceschetti and M. C. Troparevsky, *J. Phys. Chem. C*, 2007, **111**, 6154–6157.

34 D. Oron, M. Kazes, I. Shweky and U. Banin, *Phys. Rev. B: Condens. Matter Mater. Phys.*, 2006, **74**, 115333.
35 I. Robel, R. Gresback, U. Kortshagen, R. D. Schaller and V. I. Klimov, *Phys. Rev. Lett.*, 2009, **102**, 177404.
36 A. F. Cihan, Y. Kelestemur, B. Guzelturk, O. Yerli, U. Kurum, H. G. Yaglioglu, A. Elmali and H. V. Demir, *J. Phys. Chem. Lett.*, 2013, **4**, 4146–4152.
37 C. B. Poitras, M. Lipson, H. Du, M. A. Hahn and T. D. Krauss, *Appl. Phys. Lett.*, 2003, **82**, 4032–4034.
38 S. F. Wu, S. Buckley, J. R. Schaibley, L. F. Feng, J. Q. Yan, D. G. Mandrus, F. Hatami, W. Yao, J. Vuckovic, A. Majumdar and X. D. Xu, *Nature*, 2015, **520**, 69–U142.
39 E. M. Purcell, *Phys. Rev.*, 1946, **69**, 681–681.